fluids

MDPI

Article

Air Knives: Going Beyond the Classical Midspan Pressure Distributions

Celia Miguel-González [1], Aitor Vega-Valladares [2], Manuel García-Díaz [2], Alejandro Rodrígurez de Castro [1], José González Pérez [2] and Bruno Pereiras [2,*]

[1] ArcelorMittal Global R&D Asturias, P.O. Box 90, 33400 Avilés, Spain; celiamiguelg@gmail.com (C.M.-G.); alejandro.rodriguez-decastro@arcelormittal.com (A.R.d.C.)
[2] Área de Mecánica de Fluidos, University of Oviedo, Campus de Viesques, 33271 Gijón, Spain; vegaaitor@uniovi.es (A.V.-V.); garciadmanuel@uniovi.es (M.G.-D.); aviados@uniovi.es (J.G.P.)
* Correspondence: pereirasbruno@uniovi.es

Abstract

Air knives are extensively employed in many cold rolling or tin plate production lines for drying purposes. Generally, these systems are oversized, resulting in excessive energy consumption, a consequence of insufficient understanding of their performance. Considering this deficiency, an empirical exploration was initiated to analyze the functionality of an air knife oriented perpendicularly to a given surface. Given the scarcity of information within the current body of literature, particular emphasis was placed on the regions affected by the finite dimensions of the device. Impingement pressure distributions were measured at the midspan plane and planes parallel to the midspan but extending beyond the projection of the air knife. The midspan impingement pressure profile aligned with the established bell-shaped distribution, whereas the outcomes beyond the air knife's projection conformed to an analytically fitted similarity principle. Consequently, the mathematical formulations introduced in this study facilitate the mapping of the impingement pressure within the whole impingement plane, encompassing areas influenced by the finite length of the air knife, thereby representing the innovative contribution of this research.

Keywords: planar jet; nozzle; wiping; pressure distribution; edge-effect similarity

1. Introduction

One of the main challenges in the manufacturing sector is developing more efficient processes, aiming to reduce both energy consumption and the wastage of raw materials. This endeavor will facilitate the decarbonization of the industry and enable compliance with international climate targets.

Numerous industrial sectors require procedures that involve the utilization of liquids for purposes such as cleaning, cooling, lubrication, and coating. These liquids must be entirely or partially eliminated once their intended function has been fulfilled, as inadequate drying or wiping can significantly increase product rejection rates. Consequently, the development of more efficient drying and wiping systems to avoid product rejection, while minimizing energy consumption, is a crucial objective for most industries [1].

In cold rolling mills, insufficient drying of the emulsion used for cooling and lubrication can lead to the formation of emulsion stains (Figure 1). These stains typically appear when unwinding strips after being coiled with liquid residues on their surfaces. The hues of these stains vary from brown to black, exhibiting a pronounced prevalence at strip

Check for updates

Academic Editor: Tongming Zhou

Received: 5 February 2026
Revised: 13 April 2026
Accepted: 28 April 2026
Published: 30 April 2026

Copyright: © 2026 by the authors. Licensee MDPI, Basel, Switzerland. This article is an open access article distributed under the terms and conditions of the Creative Commons Attribution (CC BY) license.

edges. Although this issue is primarily aesthetic, it is unacceptable in sectors such as the automotive and household appliance industries. Indeed, this is a common cause for product rejection, resulting in significant financial losses. For illustrative purposes, the rejections attributable to this particular defect within a conventional cold rolling mill could amount to €1 million per year. Consequently, given the critical role of drying systems in these processes, drying systems are typically over-engineered, leading to excessive energy consumption.

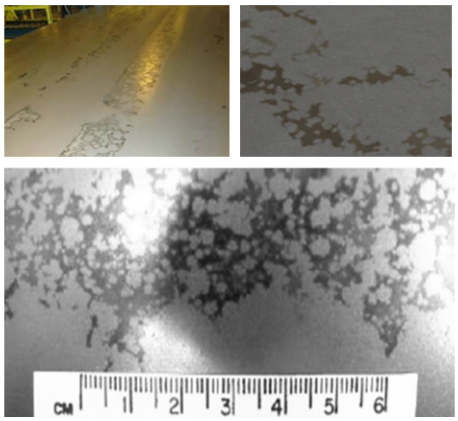


Figure 1. Emulsion stains in steel products obtained after cold rolling.

Currently, methodologies for liquid extraction systems can be categorized into two main types: wiping systems and drying systems. The selection between these methods is largely determined by the thickness of the liquid layer that requires elimination (Figure 2). On the other hand, both types of systems are often employed in certain production lines [2].

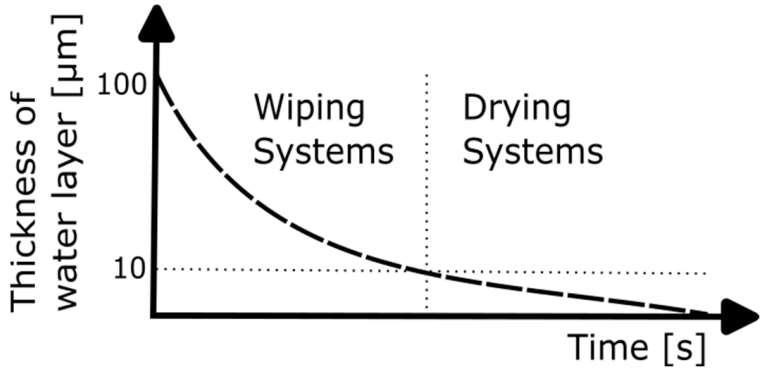


Figure 2. Type of liquid removal systems depending on the water thickness.

In wiping systems, air blowers and wringer rollers are commonly used in various manufacturing sectors, including steel production, microelectronics, pharmaceuticals, and display manufacturing, among others. Focusing on gas blowers, a fundamental method for removing liquid from surfaces involves the utilization of planar jets, which are positioned orthogonally [3], inclined [4,5], or parallel [6] to the surface. These devices are widely employed in many processes for three main purposes:

- Moisture drying, using hot air. For example, for the food or paper industry [2].
- Obtaining products with a specific coating thickness, such as in hot-dip galvanizing lines [7–9] or solar cells [10].
- Cooling [11,12].
- Removing fluids from a surface, such as in cold rolling or tinplate manufacturing lines [13].

The main differences are the existence of film breakage [14] or using cold air in the third case.

The particular case of a perpendicular impinging planar jet has been extensively studied by several authors. All the works related to this topic mention two different regions of the jet: the impinging jet and the wall jet, as can be seen in Figure 3, where D is the nozzle width, U_o is the velocity at the nozzle outlet, H is the blowing distance, and τ is the wall shear stress.

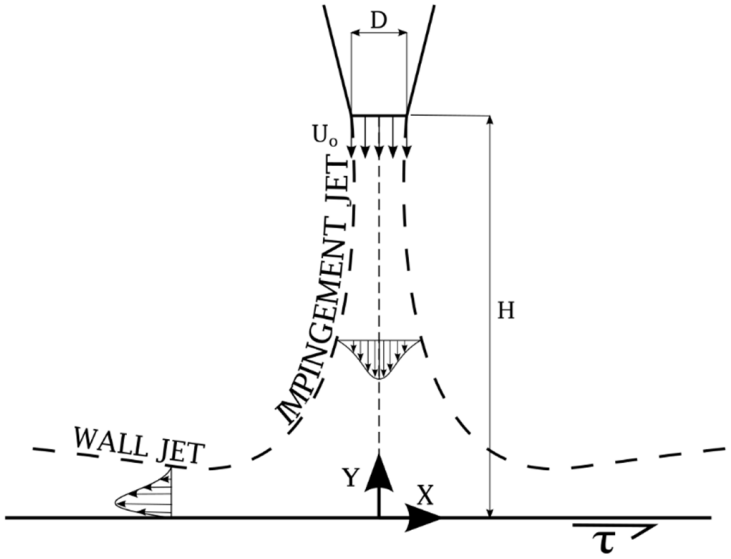


Figure 3. Planar air jet impinging perpendicularly on a flat surface. Definition of the main regions: impinging jet and wall jet.

The earliest bibliography related to perpendicular impinging planar jets was primarily focused on developing correlations to analytically reproduce the velocity, pressure and shear stress field associated with the jet. These correlations were subsequently employed in analytical models to predict liquid thickness in hot-dip galvanized lines, assessing heat transfer coefficients, etc. Multiple references can be found on this topic, e.g., [15,16].

Although basic research on this area continues, most efforts have branched out in different directions. Significant attention has been devoted to analyzing the interaction between the jet and liquid free surfaces [17–19]. Additionally, many studies have explored the design of complex nozzles aiming to reduce flow instabilities and improve performance [20,21]. And other researchers have diverted their interest to achieve a better understanding of the flow structures associated with the intrinsic instabilities of a free jet [22–27].

When an air jet impinges on a surface, its operation is inevitably related to the impingement pressure distribution generated on the surface. Ref. [16] conducted an investigation into the impingement pressure distribution associated with a planar jet across various H/D ratios (Figure 3). It was concluded that an increase in the H/D ratio results in an expansion of the impingement region's width, while reducing the maximum pressure value. This phenomenon occurs such that the integral area beneath the pressure curve, which represents the force per unit width, remains nearly constant to maintain equilibrium with the momentum of the jet. Consequently, it is evident that all parameters exhibit adherence to a dimensionless profile. Furthermore, multiple researchers indicate that the maximum impingement pressure is independent of the Reynolds number [16,28].

However, concerning wiping systems employed in industrial settings, it should be noted that most of the commercially available air knives are characterized by a hollow internal structure. It is crucial to understand that these systems are commonly engineered with

an emphasis on simplicity: slots machined into cylindrical tubes or bent plates accompanied by welded side covers. The focus is on reducing both manufacturing and maintenance expenses. Additionally, these systems are frequently retrofitted into existing facilities, requiring modifications that have not been rigorously validated by the manufacturers, potentially leading to operational failures [29].

As noted, emulsion stains appear mainly at the strip edges, indicating a malfunction of the air knife in those areas. Although there are studies that analyze tridimensional effects within the planar jet created by an air knife [22–27], they are mostly focused on turbulent instabilities. Therefore, there is no available information in the literature regarding the performance at the side of a finite planar jet.

This investigation analyzes a commercial air knife, focusing on the performance at the lateral sides where deviations from the two-dimensional performance are expected. An experimental campaign was conducted to measure impingement pressure profiles along the entire span of the air knife, specifically encompassing areas that extend beyond the vertical projection of the air knife itself. To the authors' knowledge, this subject has not been previously investigated and could significantly enhance existing knowledge of air knife performance, as it enables researchers to make reliable predictions in regions where traditional two-dimensional approaches are not fully adequate.

The results indicate that the impingement pressure fields beyond the lateral boundaries of a finite air knife follow a similarity law based on an exponential correlation. This formulation, in combination with established correlations for planar jets, enables the prediction of impingement pressure profiles associated with a finite-length air knife. The output of this work could lead to potential improvement in the efficiency of any finite air knife system, as well as support the development of more reliable analytical models for industrial processes.

Note that all the experimental measurements are available at the University repository [30].

2. Experimental Set-Up and Measurement Methodology

2.1. NCRig Facility

A test bench (Figure 4), named the Nozzle Characterization Rig (NCRig), was built at the Fluid Mechanics Laboratory of the University of Oviedo in order to measure pressure profiles and shear stress distributions of wiping systems, including impinging planar jets.

The NCRig is equipped with a three-axis (XYZ) movement system aligned by guides and driven through spindles by bipolar stepper motors (NEMA23 (Usongshine, Shenzhen, China) for the Z axis and NEMA 17 (Shenzhen Longruner Digital Co., Ltd., Shenzhen, China) for the X and Y-axis). For the motor control, drivers DRV8825 were employed. In addition, two endstop switches (WJMY) were implemented per axis to limit the movement. For the whole system control, an open-source hardware composed of an Arduino equipped with a Shield RAMPS 1.4 was used.

The installation is fed by a stationary electric compressor ER-15 from Betico (Vitoria-Gasteiz, Spain), which offers regulation capabilities ranging from 0.5 to 2.5 m^3/min and pressure adjustments between 6 and 13 bar; it also encompasses instrumentation for the acquisition of impingement pressures, flow rates, velocities, and shear stress values.

For this work, an air knife (see Figure 5), with a span (L) of 160 mm and a nozzle width (D) of 2.1 mm, was used for the tests. The ratio $L/D \approx 80 > 60$, according to the literature [16], guarantees a planar jet at the midspan. This air knife is characterized by two main features:

- It is double-fed. This configuration was chosen since previous studies on air knives fed from one side showed a clear deficit in uniformity in the velocity field at the nozzle

outlet [29]. The double-fed configuration presents smaller deficits [31,32] and, in this work, a non-frontal arrangement of both inlets was selected.

- Since this work is focused on industrial applications, the model emulates a conventional commercial configuration. It was constructed without internal honeycombs, which would be expected to increase turbulence in the shear layers, leading to larger flow entrainment and faster jet spreading.

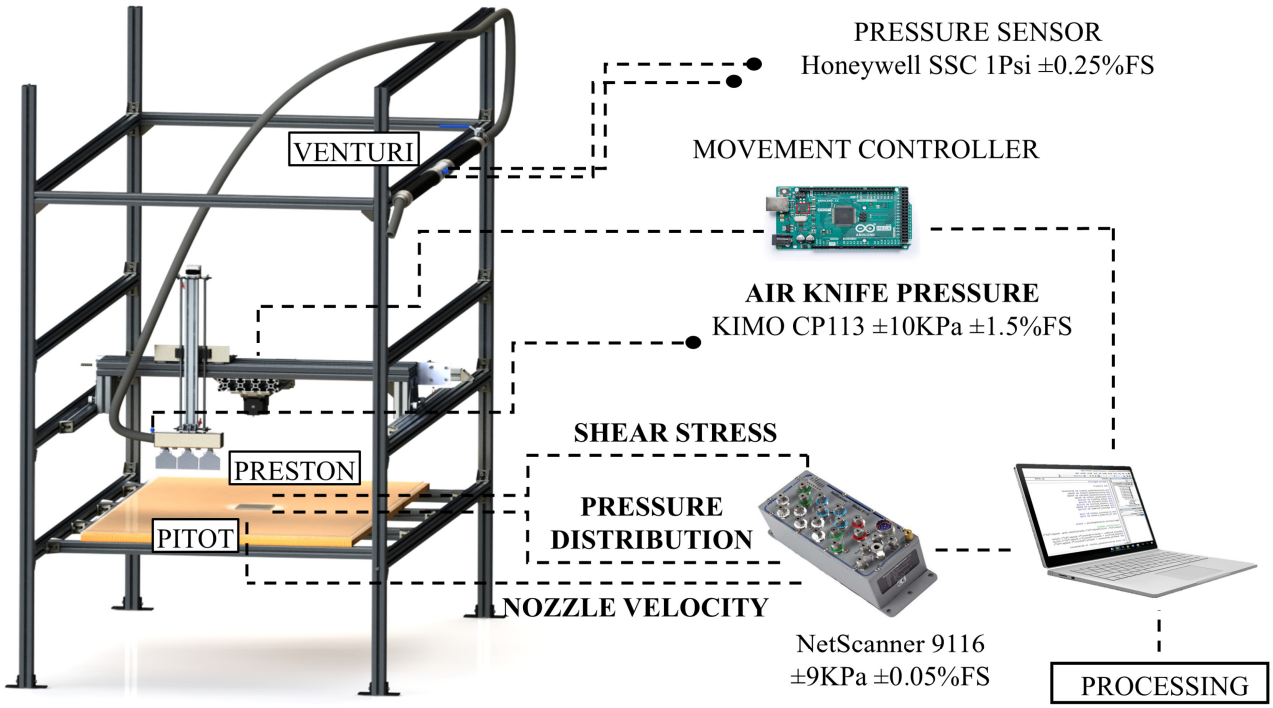


Figure 4. NCRig frame and instrumentation. Air knives or arrays of nozzles can be tested.

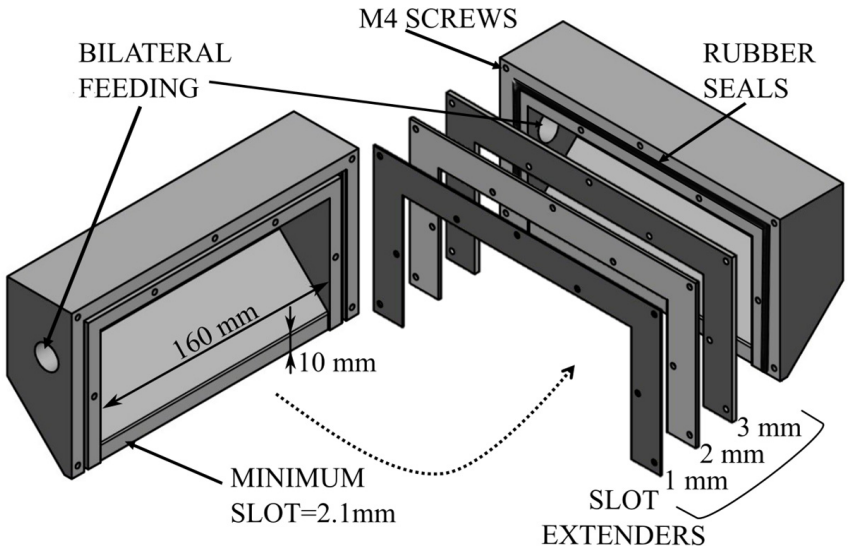


Figure 5. Geometry of the air knife. This work was carried out using the first extender of 1 mm.

In all the experimental assessments conducted for this investigation, the planar jet was oriented perpendicularly to the surface. Furthermore, a methacrylate plate measuring 1200 × 600 mm^2 was situated at the center of the rig to serve as the impingement surface for the experimental trials.

2.2. Pressure Measurements

The results obtained from the tests have been made dimensionless using the classical formulation in function of the dynamic pressure at the nozzle outlet: $P/0.5\rho U_o^2$. Note that U_o is the velocity measured at the air knife midspan.

U_o was assessed through two distinct methodologies: (1) Assuming stagnation within the air knife and applying Bernoulli's principle to the static pressure present, and (2) employing a simple Pitot tube (G27-gauge needle) at the nozzle's outlet. Although the discrepancies in values remain below 2%, the authors ultimately resolved to utilize the measurement obtained from the Pitot tube, as the absence of a honeycomb structure within the air knife could potentially result in an incomplete stagnation zone surrounding the static pressure tap.

The width of the pressure profile is an additional parameter utilized in the post-processing phase. Figure 6 illustrates the method employed to determine this measurement. It is defined from the position at which the pressure value equals one-half of the maximum value recorded at the impinging point. The values for each case are reported in Table 1.

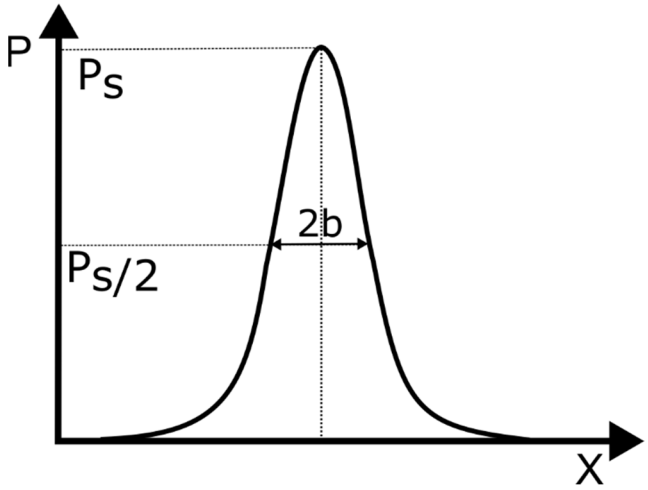


Figure 6. Determination of the pressure profile width (2b) as a function of the stagnation pressure in the impingement point.

Table 1. Test matrix.

P_c [kPa]	H/D	U_o [m/s]	Re	b [mm]
1	[4, 12, 20.6]	43.6	6.1×10^3	[2.22, 4.20, 6.19]
2		62.2	8.8×10^3	
3		76.2	11×10^3	

The measurements were made at different blowing distances H/D (Figure 3) within the range of [4–22.4], whereas the static pressure inside the air knife was set to P_c = [1, 2, 3] kPa. These P_c values drive the jet to reach velocities $U_o < 76$ m/s and the Re number to be in the range of 6000–11,000. Note that the Re is defined in terms of the nozzle width (D) and U_o. The temperature at the nozzle outlet was also measured to assess the air density. Table 1 summarizes the operational parameters used in the tests.

Flow conditions in Table 1 fall within the range encountered in industrial processes, as reported in the literature. Reference [31] indicates that, in galvanizing lines, gas jet velocities lie between 50 and 200 m/s. Reference [33] reports the use of velocities around 100 m/s in the manufacturing of organic and hybrid semiconductor thin films, and, in

the context of perovskite solar cell fabrication, ref. [34] employs air knives operating at velocities below 40 m/s.

Impinging pressure profiles were obtained using the 16 pressure taps of 0.9 mm in diameter, separated by 2 mm from each other, along OX direction (Figure 7). The air knife was systematically maneuvered along the OX-axis to make measurements every 0.25 mm, thus having 128 measurement points in OX in each Z-position. To evaluate the pressure field throughout the entire span of the air knife, the movement system adjusted the air knife by 1 mm between measurements along OZ′ direction at the lateral sides, while larger displacements were implemented as the system approached the midspan.

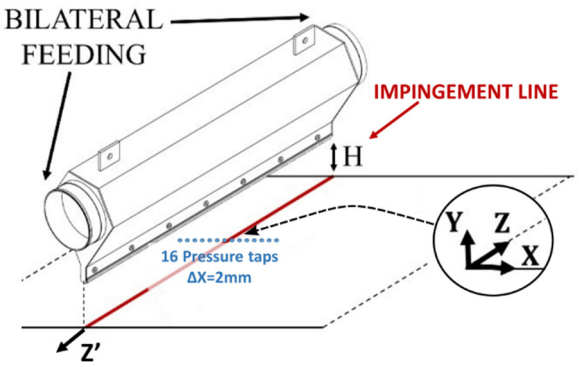


Figure 7. Sketch of the blowing system. Relative position of the pressure taps for the static pressure measurements.

Measurements were taken along the entire length of the nozzle projection, extended by an additional 40 mm, with the first and last measurement positions located 20 mm outward from the projection. Data at each measurement point was recorded for a minimum of 30 s in order to: (a) discard the initial five seconds and avoid transient effects caused by the displacement of the air knife, and (b) perform time-averaging to smooth out any unsteadiness associated with the vorticity at the nozzle outlet.

2.3. Instrumentation

A 16-port pressure scanner (NetScanner 9116 (Pressure Systems, Inc., Hampton, VA, USA), range of ±9 kPa and error of ±0.05% FS) was employed to measure the static pressures at the pressure taps to determine the impingement pressure distribution. The sampling frequency of the scanner was set to 100 Hz throughout the entire study.

The static pressure inside the air knife was assessed by a KIMO CP113 (KIMO Instruments, Montpon-Ménestérol, France) with a measurement range of ±10,000 Pa and an accuracy of ±1.5% of the reading plus ± 30 Pa.

An uncertainty analysis of the measurements was carried out following the Kline methodology [35], taking into account the resolution of the equipment used to obtain the pressure. Table 2 shows the relative uncertainties of each variable for the dimensionless values of pressure impingement. It is clear from the data that the measurement of the outlet velocity U_o, reaching 1.5% of relative uncertainty, constitutes the most significant contribution to the overall uncertainty.

Table 2. Relative weight (%) of each variable uncertainty when assessing the dimensionless values of the impingement pressure profile $P/0.5\rho U_o^2$.

Parameter \ Variable	$\frac{u(D)}{D}$	$\frac{u(L)}{L}$	$\frac{u(U_o)}{U_o}$	$\frac{u(\rho)}{\rho}$	$\frac{u(P)}{P}$	**Combined Relative Uncertainty**
$P/0.5\rho U_o^2$	0.50	≈0	1.50	0.50	0.2	1.67

3. Results and Discussion

3.1. Impingement Pressure Profiles at Midspan

Figure 8 shows the corresponding impingement pressure profiles for some of the cases tested, encompassing three H/D and three different P_C in the air knife (see Table 1). As anticipated, the results follow the established Gaussian distribution when normalized by the stagnation pressure recorded in each profile. This correlation has been documented in numerous prior studies as:

$$P/P_s = e^{-\alpha(X/b)^2} + f(X/b) \quad (1)$$

where both the coefficient α and the function f depend on the reference. Note that from a physical standpoint, α can be interpreted as a measure of the lateral momentum redistribution induced by turbulent mixing and is therefore directly related to jet spreading and air entrainment mechanisms. Taking into account the absence of honeycomb, it should be expected that α values would be smaller than in the literature, especially those where the air knife is involved with numerous elements (perforated plates, screens, etc.) to reduce turbulence, e.g., [15,16]. However, all the results of this investigation align remarkably well with the coefficients provided by [16], $\alpha_{mid} = -Ln\left(\frac{1}{2}\right) \approx 0.69$, reaching an agreement of R^2 coefficient of 0.9812. The fact that the dimensionless impingement pressure field appears to be unaffected involves the lack of honeycomb, which is partially compensated for. Here, the authors consider that the ratio between the lip length and the nozzle gap (≈4.7) is enough to suppress transversal velocities and reach a stabilized top-hat velocity profile [36].

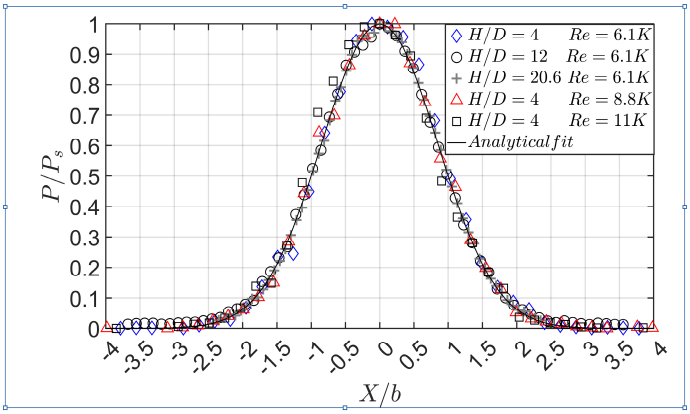


Figure 8. Normalized pressure profiles for the tested cases in Table 1. Some data of each series have been suppressed for clarity. Some profiles, which perfectly match the shown data, have also been suppressed for clarity. Analytical fit corresponds to Equation (1) from [16].

On the other hand, the large ratio between the lip length and the nozzle gap has a side effect. While it stabilizes the flow, it also promotes a more pronounced boundary layer growth, generating viscous losses and increasing the displacement thickness along the lips, which reduces the jet's core velocity.

As a consequence, downstream of the nozzle exit, the width of the jet increases while the potential core length diminishes [16,26], leading to a reduction in the stagnation pressure. Consequently, when comparing the results to the literature, an underestimation of the maximum impingement pressure P_s is observed. It increases with H/D and reaches a deficit of 10% for the largest H/D tested.

According to [16], the influence of the upstream turbulence is appreciated from distances $H/D \gtrsim 3$, which is in agreement with the results of this work. Although further

investigations should be made to evaluate the dependency on the level of upstream turbulence and lip length, the data obtained in this work, for $H/D \geq 4$, follow the proposed fitting expression: $P_s/\left(0.5\rho U_o^2\right) \cong -log(H/D) + 1.55$.

From these findings, it is concluded that the absence of the honeycomb is affecting the value of the maximum impingement pressure, but the dimensionless profile for all the cases is unaffected. Therefore, this expression is recommended for applications where no honeycomb is incorporated within the air knife, provided the nozzle geometry is such that a top-hat velocity profile is reached.

In addition, it is also seen that there is independence of the Reynolds number within the ranges analyzed (Table 1) in the three H/D distances studied, in agreement with many references, e.g., [15,16].

3.2. Span-Wise Distribution of Maximum Impingement Pressure

Figure 9 is focused on one of the objectives of this work. It shows the evolution of the maximum impingement pressure registered during the scanning process along the impingement line situated on the *OZ*-axis for the specific case of $H/D = 12$ and $P_c = 2$ KPa. As expected, the performance is almost 2D within the central 90% of the air knife. However, there is a local bump on the left side across all cases, resulting in a deviation that ranges from 4% to 6% relative to the midspan, depending on the case. It was determined that it was created by a change in the feeding pressure because it appears in all the tests and in the same location. The width of the air knife was checked by a caliper, finding that the difference in width along the whole span was less than 2.5%. Thus, since similar deviations are shown in [31] for a double-fed air knife, the hypothesis of the authors is that this deviation is related to the absence of any honeycomb and the interaction between the inlet jets, which are placed just in front of each other. Nevertheless, the authors acknowledge that further studies in this research line should corroborate this hypothesis. Despite the pressure differential remaining below 6%, it is suggested that the design methodologies employed by the majority of air knife manufacturers (not including a honeycomb) may lead to certain deviations from the ideal 2-D operational performance.

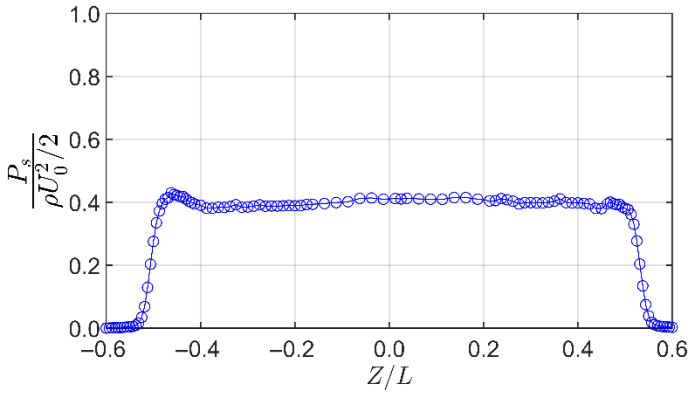


Figure 9. Maximum dimensionless impingement pressure along *OZ* direction for $H/D = 12$ and $Re = 8.8$ K.

The degree of uniformity in the pressure field, closely related to the double-fed air knife, must be taken into account when analyzing the forthcoming results. Note that any deviation from this degree of uniformity, e.g., in single-side-fed air knife, would lead to results different from those reported in the following sections.

3.3. Impingement Pressure Profiles at Air Knife Lateral Boundaries

As shown in Figure 9, the gradients at the air knife sides are unexpectedly large. The extent of the jet's impingement is merely 10% greater than the length of the nozzle. Focusing on the gradients at the sides, several noteworthy conclusions can be deduced. From Figures 10–12, the impingement pressure profiles for different Z'-coordinate positions in the tests with $H/D = [4, 12, 20.4]$ for $Re = [6.1,\ 8.8,\ 11] \times 10^3$ are shown. The data were collected starting from 1 mm within the projection of the nozzle and moving outwards. Coordinate Z' can be seen in Figure 7.

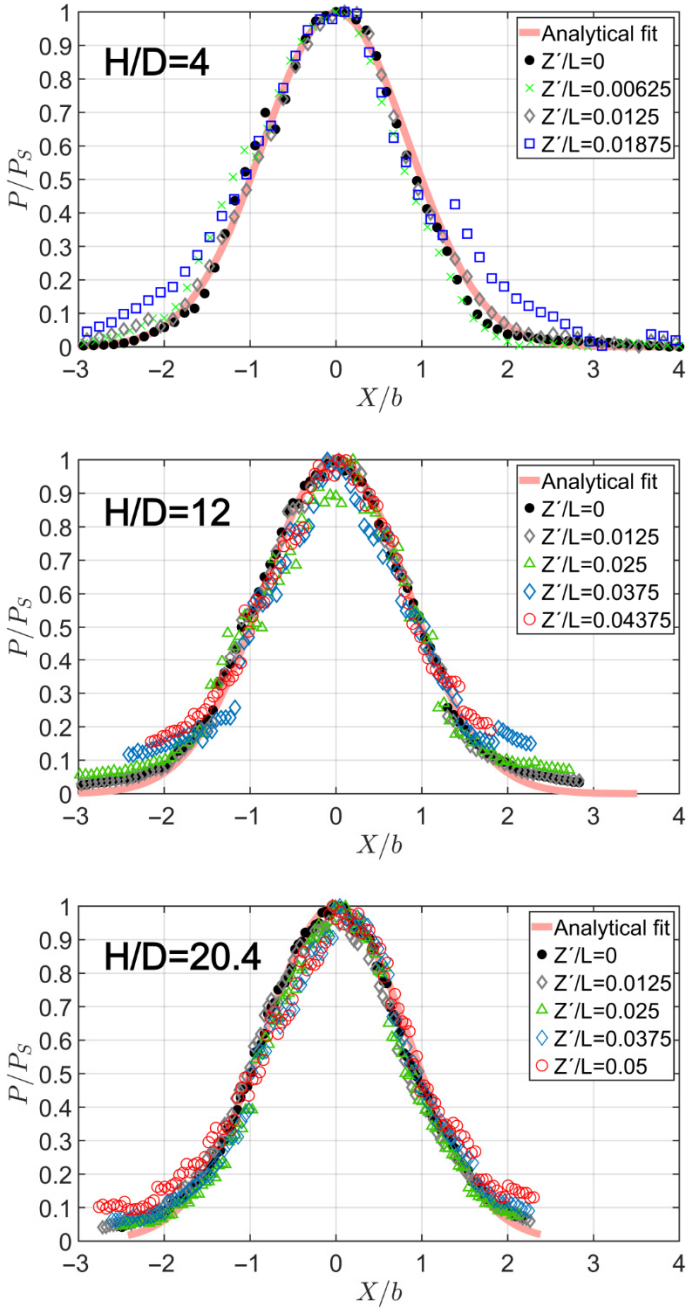


Figure 10. Pressure profiles for various locations at the air knife side for $Re = 6.1$ K, right side. Half of the data of each series have been suppressed for clarity.

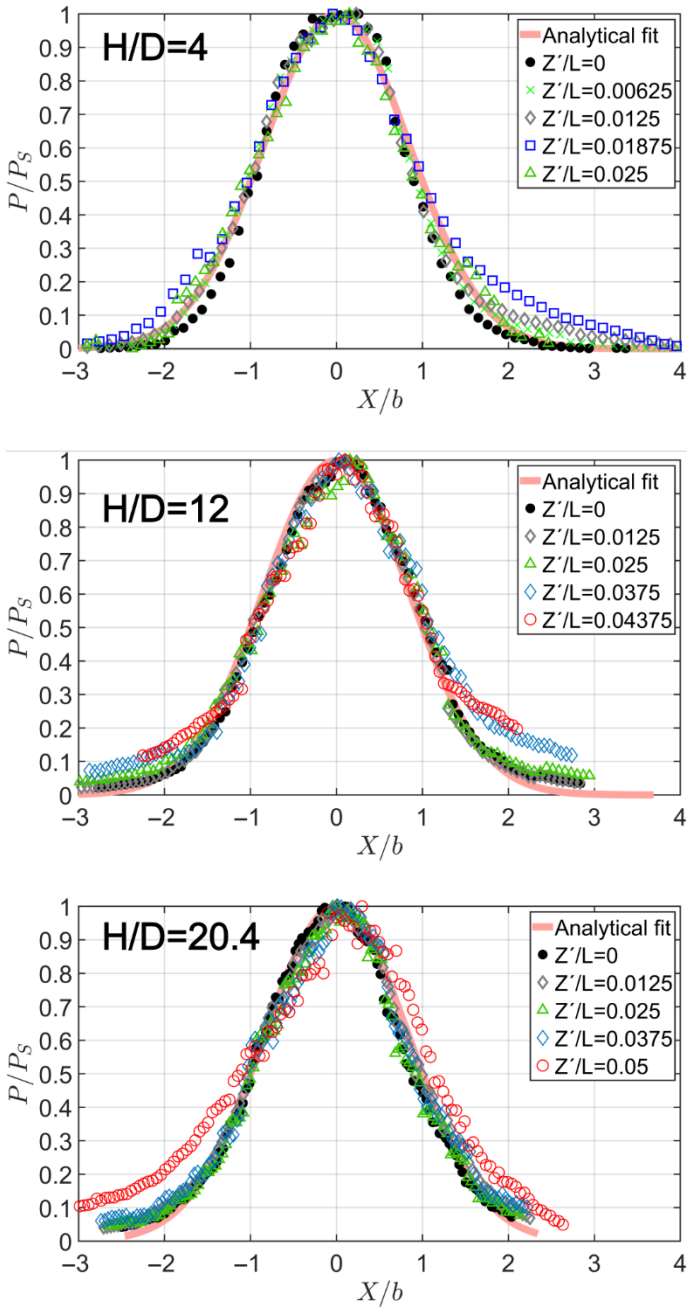


Figure 11. Pressure profiles for various locations at the air knife side for $Re = 8.8$ K, right side. Half of the data of each series have been suppressed for clarity.

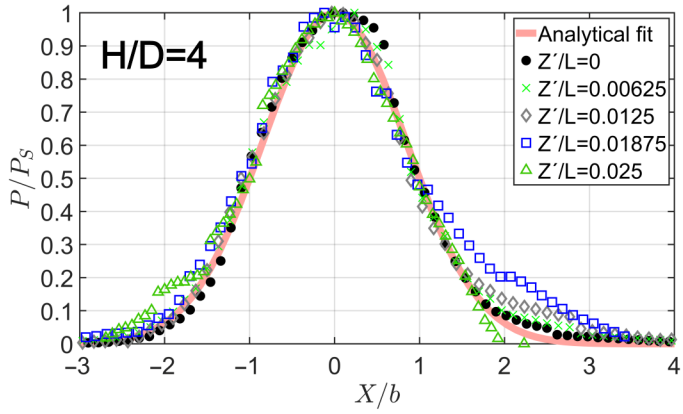


Figure 12. *Cont.*

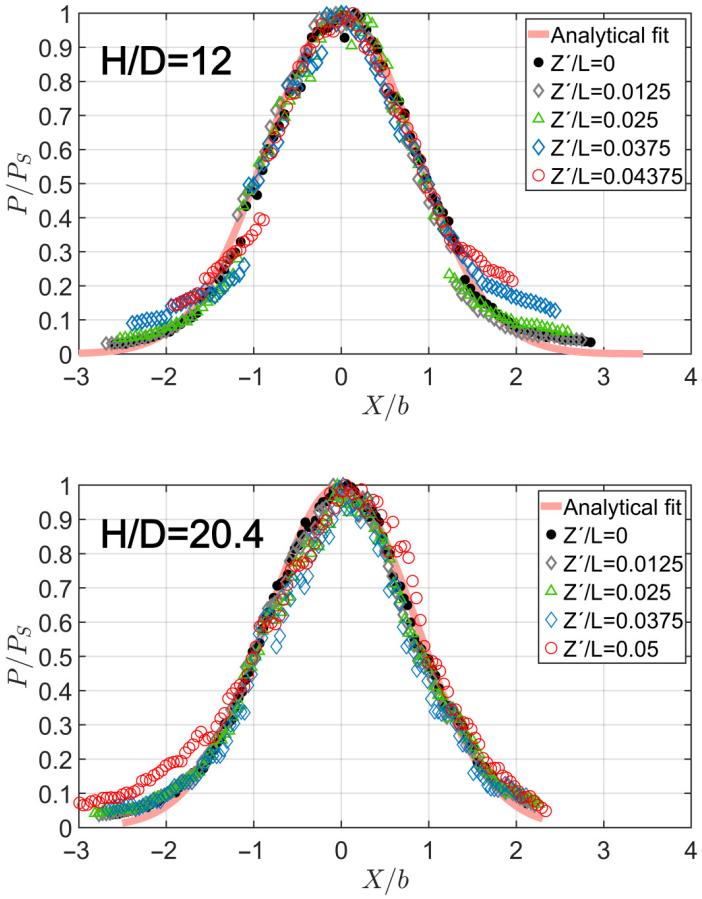


Figure 12. Pressure profiles for various locations at the air knife side for $Re = 11$ K, right side. Half of the data of each series have been suppressed for clarity.

It should be noted that the results presented in Figures 10–12 correspond to the right side of the nozzle. Nevertheless, the authors would like to remark that the deviation between the left and right sides does not exceed ±2.5%. To avoid redundancy, only the results from the right side are presented.

Note that in cases of $H/D = 4$, since the nozzle is closer to the surface, the spreading of the jet in Z' direction is extended no more than 3 or 4 millimeters before the measured pressures are negligible. Thus, a lower number of pressure profiles are available in the top-of-figure subplots in Figures 10–12. On the other hand, more data series are available for larger H/D values, but certain series have been omitted for clarity.

From comparing Figures 10–12, it is confirmed that the whole set of pressure profiles presents an evident similarity. They follow a similar law to the one at the midspan (Equation (1), extracted from [16]), only changing the maximum impingement pressure, which depends on the Z'-coordinate. Only minimal deviations were registered where the pressure approaches the uncertainty of the measurement process, which occurs at the largest Z'/L values and at the limit of the impingement region (large $|X/b|$). Comparing the experimental data with Equation (1), the agreement is excellent with R^2 ranging from 0.9574 to 0.9865. The fact that the pressure profiles at the side boundaries match the same expression used for midspan is a finding not yet reported in the literature, to the authors' knowledge.

On the other hand, the value of P_S for each profile measured at different Z'-coordinates also exhibits similarity. Figure 13 presents the dimensionless ratio between the maximum impingement pressure of each profile at the designated Z'-coordinate positions and the maximum pressure recorded at the midspan, which functions as the reference point. All the

tests are included in this picture. Since this variable is closely related to the jet spreading, the data should match an expression of the same type as planar or round jets. Accordingly, the values adhere to a distinct trend that can be approximated by an expression of the form:

$$P_s / P_{s\ mid} = e^{-\alpha (Z'/b')^2} \tag{2}$$

where b' is measured as shown in Figure 6, but in Z'-coordinate, from $Z' = 0$ up to the location of half-maximum pressure. The results agree very well with the proposed expression, reaching an excellent $R^2 = 0.9399$ when $\alpha = \alpha_{mid} = -Ln(1/2) \approx 0.69$. Thus, the pressure impingement profiles at the midspan in XY-plane, the pressure profiles at the lateral boundaries of the air knife in XY-planes for different Z'-coordinates, and the impingement pressure profile in the XZ-plane can be expressed using the same equation. This is surprising since it is known that rectangular free jets of large aspect ratios, see [37,38], register an almost negligible growth in the Z-coordinate, in contrast to the transverse spreading, which increases almost linearly. This difference in the lateral spreading compared to other works, also observed in other research on rectangular free jets, is attributed to the nozzle geometry [37,38]. See those references for more information about the spreading phenomena.

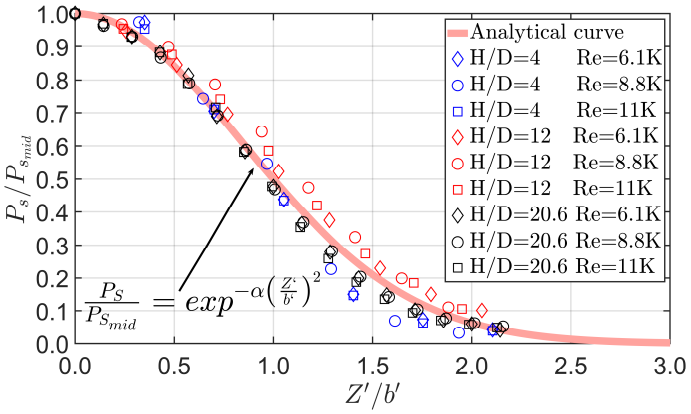


Figure 13. Normalized profile maximum pressure for different locations Z'/b' at the side of the nozzle.

Consequently, the impingement pressure profile can be characterized along the entire span of the air knife, including regions beyond the lateral boundaries, using mathematical formulations. Therefore, these findings assert that, once the exit velocity of the nozzle is evaluated, the mathematical expressions provided yield precise predictions of the pressure distribution of an air knife of finite length.

4. Conclusions

Experimental tests of an air knife blowing perpendicularly against a flat surface have been carried out in the present work. In addition to the conventional measurements of impingement pressure in the midplane, novel measurements were conducted to characterize the performance at the lateral sides of the impingement jet. This approach allowed us to evaluate the limitations associated with three-dimensional effects resulting from the finite length of the air knife. The test campaign covered different values of the ratio H/D and the Re number to analyze a wide range of performance conditions.

Pressure profile measurements at midspan follow the well-known bell-shaped structure previously reported in the bibliography. On the other hand, the measurements at the sides of the impingement jet have unveiled interesting facts. Pressure profiles at these lateral regions show a clear similarity, which facilitates their analytical determination through mathematical expressions. The main finding of this work is that the impingement pressure

profiles at the lateral boundaries of the jet agree extremely well with the same expression at the midspan.

Consequently, it becomes feasible to quantitatively characterize the pressure profiles within the impingement zone across the entire span of an air knife, encompassing areas influenced by the three-dimensional effects resulting from the finite length of the air knife. These findings highlight a characteristic that has not been previously documented in existing literature.

Nevertheless, the conclusions of this work should be extended beyond the specific geometry and operating conditions of the tested configuration with caution. Additional experiments covering a wider range of H/D values, Reynolds numbers, and turbulence levels would provide further support for the conclusions drawn.

Author Contributions: Conceptualization, B.P. and J.G.P.; methodology, B.P.; software, C.M.-G. and A.V.-V.; formal analysis, C.M.-G. and J.G.P.; investigation A.V.-V.; resources, A.V.-V., M.G.-D. and A.R.d.C.; data curation, A.V.-V. and C.M.-G.; writing—original draft preparation, M.G.-D. and A.V.-V.; writing—review and editing, B.P. and M.G.-D.; visualization, M.G.-D.; supervision, B.P. and J.G.P.; project administration, J.G.P. and B.P.; funding acquisition, A.R.d.C. All authors have read and agreed to the published version of the manuscript.

Funding: Miguel-González, C. was supported by the Spanish "Ministerio de Educación Cultura y Deporte" within the "Doctorados Industriales" Program (grant number DI-17-09596). García-Díaz, M. was supported by the Spanish "Ministerio de Educación, Cultura y Deporte" within the "FPU" Program (grant number FPU15/04375). Vega-Valladares, A. was supported by the "Administración del Principado de Asturias" within the "Severo Ochoa" Program (grant number BP-21-160).

Institutional Review Board Statement: Not applicable.

Informed Consent Statement: Not applicable.

Data Availability Statement: Reference [30] shows the initial data retrieved for the graphs shown in the present article.

Conflicts of Interest: The authors declare no conflicts of interest.

Abbreviations and Symbols

The following abbreviations and symbols are used in this manuscript:

b, b'	Half-width of impingement pressure profile [mm], XY and XZ' planes.
D	Nozzle width [mm].
$d_{out/in}$	External/internal diameter of the Preston tubes [mm].
H	Blowing distance [mm].
K	For the Re in Figures 7 and 12, meaning a factor of 1000, or $\cdot 10^3$.
L	Air knife span [mm].
P	Pressure [Pa].
P_c	Static pressure inside the air knife [Pa].
P_s	Profile maximum impingement pressure [Pa].
ΔP_P	Total-to-static pressure difference between Preston tube inlet and the static pressure at its position [Pa].
P_t	Stagnation pressure measured at the Preston tube inlet [Pa].
$Re = U_O D/\nu$	Reynolds number.
U_O	Velocity at the nozzle outlet [m/s].
$U(x)$	Uncertainty of variable x.
X, Y, Z, Z'	Coordinates.
Greek symbols:	
ρ	Density [kg/m^3].
ν	Kinematic viscosity [m^2/s].

α, β	Coefficients of the analytical fits.
Subscripts	
max	Maximum.
mid	Midspan.

References

1. Mujumdar, A.S. An Overview of Innovation in Industrial Drying: Current Status and R&D Needs. *Transp. Porous Media* **2007**, *66*, 3–18. [CrossRef]
2. Mujumdar, A.S. *Handbook of Industrial Drying*; Mujumdar, A.S., Ed.; CRC Press: Boca Raton, FL, USA, 2020; ISBN 978-0-429-28977-4.
3. Ellen, C.H.; Tu, C.V. An Analysis of Jet Stripping of Liquid Coatings. *J. Fluids Eng.* **1984**, *106*, 399–404. [CrossRef]
4. Park, S.; Park, K. Air-Knife Design for Improved Drying Efficiency in Manufacturing Flat-Panel Displays. *J. Comput. Des. Eng.* **2022**, *9*, 1388–1396. [CrossRef]
5. Spooner, E.L.K.; Cassella, E.J.; Smith, J.A.; Catley, T.E.; Burholt, S.; Lidzey, D.G. Air-Knife-Assisted Spray Coating of Organic Solar Cells. *ACS Appl. Mater. Interfaces* **2023**, *15*, 39625–39635. [CrossRef]
6. Liu, K.; Liang, Q.; Qin, M.; Shen, D.; Yin, H.; Ren, Z.; Zhang, Y.; Zhang, H.; Fong, P.W.K.; Wu, Z.; et al. Zwitterionic-Surfactant-Assisted Room-Temperature Coating of Efficient Perovskite Solar Cells. *Joule* **2020**, *4*, 2404–2425. [CrossRef]
7. Lacanette, D.; Vincent, S.; Arquis, E.; Gardin, P. Numerical Simulation of Gas-Jet Wiping in Steel Strip Galvanizing Process. *ISIJ Int.* **2005**, *45*, 214–220. [CrossRef]
8. Kolecki, R.E. Lubricant Removal System for Cold Rolling Stand. U.S. Patent 4,619,126, 28 October 1986.
9. Yahyaee Soufiani, A.; Mcdermid, J.R.; Hrymak, A.N.; Goodwin, F.E. A Parametric Study of a Multi-Slot Air Knife for Coating Thickness Reduction. *ISIJ Int.* **2020**, *60*, 1040–1051. [CrossRef]
10. Cassella, E.J.; Spooner, E.L.K.; Thornber, T.; O'Kane, M.E.; Catley, T.E.; Bishop, J.E.; Smith, J.A.; Game, O.S.; Lidzey, D.G. Gas-Assisted Spray Coating of Perovskite Solar Cells Incorporating Sprayed Self-Assembled Monolayers. *Adv. Sci.* **2022**, *9*, 2104848. [CrossRef]
11. Ganatra, K.A.; Singh, D.; Mukhopadhyay, A. Experimental Study and Large Eddy Simulation of Slot Jet Impingement Cooling from Heated Cylinder Placed on Flat Plate. *Heat Mass Transf.* **2024**, *60*, 1313–1334. [CrossRef]
12. Erasmus, D.J.; Lubkoll, M.; von Backström, T.W. Jet Impingement Heat Transfer within a Hemisphere. *Heat Mass Transf.* **2021**, *57*, 931–948. [CrossRef]
13. Bini, C.; Holz, R. New Cold Mill Complex in Turkey—Technologies and Achieved Performances. In *AISTech2020 Proceedings of the Iron and Steel Technology Conference*; AIST: Warrendale, PA, USA, 2020; pp. 1163–1172.
14. Berendsen, C.W.J.; Zeegers, J.C.H.; Kruis, G.C.F.L.; Riepen, M.; Darhuber, A.A. Rupture of Thin Liquid Films Induced by Impinging Air-Jets. *Langmuir* **2012**, *28*, 9977–9985. [CrossRef] [PubMed]
15. Beltaos, S.; Rajaratnam, N. Plane Turbulent Impinging Jets. *J. Hydraul. Res.* **1973**, *11*, 29–59. [CrossRef]
16. Tu, C.V.; Wood, D.H. Wall Pressure and Shear Stress Measurements beneath an Impinging Jet. *Exp. Therm. Fluid Sci.* **1996**, *13*, 364–373. [CrossRef]
17. Cho, T.S.; Kwon, Y.D.; Kwon, S.B. A Study of the Influence of Air-Knife Tilting on Coating Thickness in Hot-Dip Galvanizing. *J. Therm. Sci.* **2009**, *18*, 262–267. [CrossRef]
18. Myrillas, K.; Gosset, A.; Rambaud, P.; Anderhuber, M.; Mataigne, J.-M.; Buchlin, J.-M. Technique for Delaying Splashing in Jet Wiping Process. *Chem. Eng. Process. Process Intensif.* **2011**, *50*, 466–470. [CrossRef]
19. Gosset, A.; Mendez, M.A.; Buchlin, J. An Experimental Analysis of the Stability of the Jet Wiping Process: Part I–Characterization of the Coating Uniformity. *Exp. Therm. Fluid Sci.* **2019**, *103*, 51–65. [CrossRef]
20. Tamadonfar, P. Numerical Investigacion of Multiple-Impinging Slot Jets in the Gas-Jet Wiping of Liquid Zinc Coatings. Doctoral Dissertation, McMaster University, Hamilton, ON, Canada, 2010.
21. Sepideh, A. Experimental Investigation of Air-Knife Geometry in Continuous Hot-Dip Galvanizing. Doctoral Dissertation, McMaster University, Hamilton, ON, Canada, 2014.
22. Tsubokura, M.; Kobayashi, T.; Taniguchi, N.; Jones, W.P. A Numerical Study on the Eddy Structures of Impinging Jets Excited at the Inlet. *Int. J. Heat Fluid Flow* **2003**, *24*, 500–511. [CrossRef]
23. So, H.; Yoon, H.G.; Chung, M.K. Numerical Study of Flow Fields and Heat Transfer Characteristics in an Impinging Slot Jet With Buckling Phenomenon. In *Proceedings of the Volume 7: Fluid Flow, Heat Transfer and Thermal Systems, Parts A and B*; ASMEDC: Washington, DC, USA, 2010; pp. 1521–1529.
24. Pieris, S.; Zhang, X.; Yarusevych, S.; Peterson, S.D. Evolution of Coherent Structures in a Two-Dimensional Impinging Jet. In *Proceedings of the 10th International Symposium on Turbulence and Shear Flow Phenomena*; TSFP: Chicago, IL, USA, 2017; Volume 1.
25. Senter, J.; Solliec, C. Flow Field Analysis of a Turbulent Slot Air Jet Impinging on a Moving Flat Surface. *Int. J. Heat Fluid Flow* **2007**, *28*, 708–719. [CrossRef]
26. Kamruzzaman, M.; Rømcke, O.; Hearst, R.J. The Impact of Upstream Turbulence on a Plane Jet. *Exp. Fluids* **2021**, *62*, 18. [CrossRef]

27. Ritcey, A.; McDermid, J.; Ziada, S. The Fluctuating Velocity Field of a Forced Planar Impinging Gas Jet. *J. Turbul.* **2018**, *19*, 798–825. [CrossRef]
28. Baydar, E.; Ozmen, Y. An Experimental and Numerical Investigation on a Confined Impinging Air Jet at High Reynolds Numbers. *Appl. Therm. Eng.* **2005**, *25*, 409–421. [CrossRef]
29. Miguel-González, C.; García-Díaz, M.; Pereiras, B.; Vigil, M.; Rodríguez de Castro, A. Numerical Model of a Planar Jet Wiping System for Continuous Strip Lines. *J. Mech. Sci. Technol.* **2021**, *35*, 2929–2938. [CrossRef]
30. Miguel-Gonzalez, C.; Vega-Valladares, A.; García-Diaz, M.; Pereiras, B. Experimental Data of an Air Knife, Pressure Fields and Wall Shear Stresses [DataSets] 2024. Available online: https://hdl.handle.net/10651/73091 (accessed on 27 April 2026).
31. Goodwin, F.E.; Dubois, M. Review on Wiping: A Key Process Limiting CGL Productivity. In *AISTech-Iron and Steel Technology Conference Proceedings*; Association for Iron and Steel Technology: Washington, DC, USA, 2012; pp. 1847–1859.
32. Wang, J.; Klinkberg, T.; Teschner, M.; Weirich, D.; Kreuznach, B. Simulation and Optimization of a Wiping Knife on the Lab Scale. In *Proceedings of the 12th International Conference on Zinc & Zinc Alloy Coated Steel Sheet (GALVATECH 2021)*; Austrian Society for Metallurgy and Materials (ASMET): Leoben, Austria, 2021.
33. Ternes, S. Consistent Control of Drying Rates of Solution Thin Films on Wafer-Sized Substrates by Dynamic Air-Knife Drying with Optimal Trajectories. *Chem. Eng. Sci.* **2026**, *327*, 123620. [CrossRef]
34. Fong, P.W.K.; Hu, H.; Ren, Z.; Liu, K.; Cui, L.; Bi, T.; Liang, Q.; Wu, Z.; Hao, J.; Li, G. Printing High-Efficiency Perovskite Solar Cells in High-Humidity Ambient Environment—An In Situ Guided Investigation. *Adv. Sci.* **2021**, *8*, 2003359. [CrossRef] [PubMed]
35. Kline, J.; McClintock, F.A. Describing Uncertainties in Single-Sample Experiments. *Mech. Eng.* **1953**, *75*, 3–8.
36. Deo, R.C.; Mi, J.; Nathan, G.J. The Influence of Nozzle-Exit Geometric Profile on Statistical Properties of a Turbulent Plane Jet. *Exp. Therm. Fluid Sci.* **2007**, *32*, 545–559. [CrossRef]
37. Krothapalli, A.; Baganoff, D.; Karamcheti, K. On the Mixing of a Rectangular Jet. *J. Fluid Mech.* **1981**, *107*, 201–220. [CrossRef]
38. Sfeir, A.A. The Velocity and Temperature Fields of Rectangular Jets. *Int. J. Heat Mass Transf.* **1976**, *19*, 1289–1297. [CrossRef]

Disclaimer/Publisher's Note: The statements, opinions and data contained in all publications are solely those of the individual author(s) and contributor(s) and not of MDPI and/or the editor(s). MDPI and/or the editor(s) disclaim responsibility for any injury to people or property resulting from any ideas, methods, instructions or products referred to in the content.